Solvation-Modulated Dispersions of reduced graphite oxide towards Binder-Free Conductive Inks

*Tuan Kien Nguyen[1, 2], Md. Joynul Abedin[1, 2, *], Naimeh Naseri[1, 2, 3], Meysam Sharifzadeh Mirshekarloo[1, 4], Olalekan Solomon Oluwole[1, 2], Petar Jovanovic[1, 2], Davide Deganello[5], Rico Tabor[2, 6], Mainak Majumder[1, 2, *]*

[1] Nanoscale Science and Engineering Laboratory (NSEL), Department of Mechanical & Aerospace Engineering, Monash University, Clayton, VIC 3800, Australia.

[2] ARC Research Hub for Advanced Manufacturing with 2D materials (AM2D), Monash University, Clayton, VIC 3800, Australia.

[3] Chair of Analytical Chemistry II, Faculty of Chemistry and Biochemistry, Ruhr University Bochum, Bochum, 44801 Germany.

[4] Ionic Industries Ltd., 2/247 Ferntree Gully Road, Mount Waverley, VIC 3149, Australia.

[5] Welsh Centre for Printing and Coating, Faculty of Science and Engineering, Swansea University, Swansea, SA1 8EN, Wales, United Kingdom.

[6] School of Chemistry, Monash University, Clayton, VIC 3800, Australia.

(*) Email: joynul.abedin1@monash.edu; mainak.majumder@monash.edu

Abstract

Conductive inks formulated from graphene-based materials are essential for translating graphene's potential into real-world applications. High-concentration inks are particularly valuable, enabling fewer deposition steps, reduced drying costs, and improved film uniformity. However, increasing graphene concentration typically leads to a steep rise in viscosity, limiting compatibility with most printing techniques. In this work, we address this challenge by compacting expanded reduced graphite oxide into dense-block reduced graphite oxide, termed DB-rGtO, allowing the formulation of stable dispersions of graphene-derived material at concentrations up to 200 $mg \cdot mL^{-1}$, while maintaining manageable flowability and deformation resistance. We demonstrate that solvation of DB-rGtO particles serves as a fundamental strategy to modulate ink viscosity, enabling property tuning at high solids content. The degree of solvation, quantified using polarised light microscopy, correlates well with viscosity predictions based on the Krieger–Dougherty model. Using nitrogen-doped expanded reduced graphite oxide as the starting material, this approach enables single-pass printed films and patterns with conductivities ranging from 5 to 10 $\Omega \cdot \square^{-1}$. Our findings establish general design rules for formulating concentrated, conductive graphene-based inks with little to no additive, adaptable across various deposition techniques for producing high-resolution, high-fidelity features.

1. Introduction

Graphene is compatible with solution-based processing, which is currently the most viable, cost-effective, and scalable method for translating graphene's exceptional mechanical, thermal, chemical, and electrical properties into next-generation technologies such as printed flexible electronics and devices [1-3]. Graphene is typically produced by breaking the weak van der Waals

(vdWs) forces between graphite layers, facilitating interlayer exfoliation for scalable solution-based processing. Two key methods have underpinned graphene production over the past decades: (i) exfoliation of graphite into graphene using surface tension-matched solvents [4], and (ii) chemical reduction of graphene oxide in solution [5]. Graphene serves as active materials in various ink formulations, allowing direct deposition onto flexible or rigid substrates through coating and printing techniques [1]. However, processing of graphene into functional inks remains a critical challenge, primarily due to the difficulty of producing high-concentration graphene dispersions [3]. Two main factors contributing to this limitation include (i) the poor stability of graphene dispersions beyond a certain concentration threshold, and (ii) the steep rise in viscosity with increasing graphene content.

The stability of dispersions is generally governed by the Derjaguin–Landau–Verwey–Overbeek (DLVO) theory, which describes how interaction energy varies with the distance between particles in a liquid medium [6, 7]. At sufficiently small separations, van der Waals (vdW) attractions can dominate over electrostatic double-layer repulsion, resulting in strong, irreversible attractions that cause particle coagulation. According to this theory, when graphene concentration in a solvent exceeds a critical threshold, nanosheets are brought into close proximity, leading to sheet aggregation or restacking. This destabilises the dispersion and renders it unsuitable for high-throughput coating and printing processes [2]. Graphene sheets are particularly prone to aggregation due to their high surface area-to-volume ratio, a consequence of their two-dimensional (2D) structure [8-10]. As a result, achieving graphene concentration sufficient for practical applications (10-100 $mg \cdot mL^{-1}$) inevitably requires stabilising additives (polymers, surfactants) and advanced processing [8, 9, 11-14], whereas traditional exfoliation

methods without stabilisers typically produce stable dispersions of less than 1-2 $mg \cdot mL^{-1}$ in common solvents [4, 15-21].

Dispersions of graphene are also disadvantaged as the slight increases in concentration can lead to dramatic rises in viscosity [8]. This once again stems from the exceptionally high aspect ratio of graphene sheets, which amplifies the excluded volume effect: each sheet excludes a disproportionately large volume around it due to its large lateral size and nanoscale thickness. This reduces the average inter-sheet distance and increases the likelihood of overlapping excluded volumes and interparticle interactions [9, 22-24]. Consequently, graphene dispersions tend to form interconnected, percolated networks even at relatively low concentrations. For example, graphene–ionic liquid dispersions have been reported to reach a critical gel concentration as low as 4.2 $mg \cdot mL^{-1}$ [25].

Overall, the intrinsic properties of graphene dispersions, particularly their limited dispersibility and poor flowability, pose significant challenges to the formulation of high-concentration inks, which are essential for coating and printing applications. Despite these limitations, achieving high graphene concentrations in ink formulations remains highly desirable for wet coating and printing processes. Higher concentrations ensure sufficient active material to form percolated particle networks, enabling the production of continuous films with improved uniformity, while reducing the need for multiple deposition steps that can compromise manufacturing accuracy and efficiency [3, 26, 27]. From a sustainability perspective, high-concentration inks also require less solvent, making them more environmentally friendly and reducing drying energy costs [8, 9]. To address dispersion and rheological challenges, many previously reported graphene inks incorporate additives such as binders. These binders serve dual functions: acting as stabilisers to improve dispersion concentration, and as rheological modifiers to adapt inks to specific coating

and printing techniques [3]. However, because binders are typically inactive materials, their inclusion inevitably dilutes the functional content of the ink and compromises the performance of the final device.

Notably, both key limitations in formulating high-concentration graphene inks, namely poor dispersion stability and steep viscosity increase, can be traced back to graphene's high aspect ratio and two-dimensional morphology. While current strategies largely depend on the use of binders, the alternative approach of modifying graphene's morphology remains relatively underexplored. In this study, we introduce an engineered graphene-derived structure, termed Dense-block reduced Graphite oxide (DB-rGtO), as an active material for preparing dispersions in various printing solvents. At concentrations exceeding 100 mg·mL-1, DB-rGtO dispersions maintain a viscosity range suitable for printing applications. Furthermore, compared to the conventional sheet-like graphene [28], the three-dimensional DB-rGtO is less vulnerable to irreversible particle stacking in dispersions. Unlike tightly stacked multilayer materials such as graphite or graphene nanoplatelets, DB-rGtO retains solvent-interactive behaviour i.e., solvation, due to the exposure of compacted graphene-like sheets. This solvation behaviour was systematically studied across different solvents, providing insight into the microstructure of DB-rGtO and its influence on the rheological characteristics of high-concentration dispersions.

The observed solvent-dependent solvation behaviour results in a wide range of rheological profiles, suggesting the feasibility of tailoring ink properties for specific coating and printing techniques without the need for binder additives. Leveraging these insights, a high-concentration, binder-free DB-rGtO ink (200 $mg \cdot mL^{-1}$) was successfully formulated. This ink enabled high-resolution screen printing on flexible substrates, producing well-defined interdigitated patterns with line widths and gap distances in the 100s of µm range.

Electrothermal characterisation of the printed DB-rGtO films demonstrated their potential for application in flexible electronic devices, such as electrothermal heaters.

2. Results & Discussions

2.1 Particle-engineering approach for DB-rGtO synthesis

We present a particle-engineering strategy to tailor graphene morphology and enable the formulation of highly concentrated dispersions (Figure 1a, b). Following thermal expansion, the expanded reduced graphite oxide (E-rGtO) exhibits a fluffy, accordion-like morphology with discernible two-dimensional sheets, which is typically associated with the process of rapid heating-induced exfoliation [29]. Subsequent ball milling subjects the E-rGtO to repeated collisions between the milling balls, jar, and graphene particles, introducing both fragmentation and compression effects. This process compacts the fluffy material into denser dense-block reduced graphite oxide (DB-rGtO), while also fragmenting larger agglomerates into smaller particles with a more compact structure (Figure 1b and Figure S1). Since the material does not conform to the conventional definition a two-dimensional graphene structure, we refer to it as being reduced graphite oxide. However, it should be emphasised that DB-rGtO is graphene-derived, comprising loosely-stacked thin sheets and pore networks confined within a microparticle framework (Figure S2 and S3). The dimensional transition from sheet-like to dense-block structure reduces the material's susceptibility to irreversible particle aggregation in dispersions, as the limited point contact associated with three-dimensional morphology considerably restricts the attractive forces [28, 30-32]. Table S1 and Figure S4 demonstrate data evidencing the minimal stacking of DB-rGtO, as compared to the sheet-like E-rGtO.

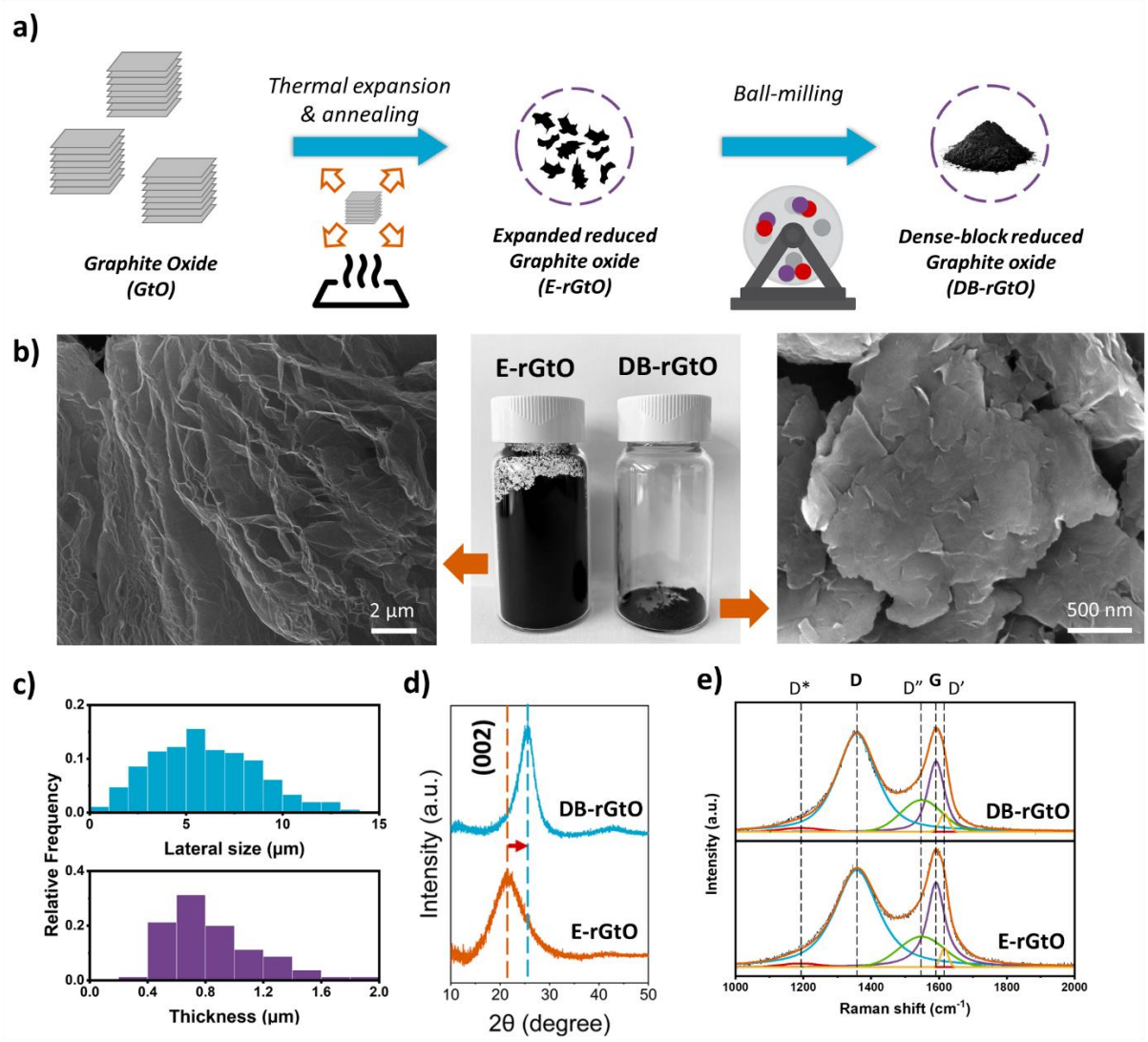

Figure 1: a) Particle-engineering approach for DB-rGtO synthesis. b) Visual comparison of expanded reduced graphite oxide (E-rGtO) and dense-block reduced graphite oxide (DB-rGtO): SEM image of E-rGtO showing accordion-like morphology with 2D sheets (left); Photograph of 80 mg of E-rGtO and 80 mg of DB-rGtO (middle); SEM image of DB-rGtO revealing 3D-dense morphology with visible graphene-like sheets on particle surface (right). c) Particle lateral size and thickness distribution of DB-rGtO material. d) XRD analysis of E-rGtO and DB-rGtO, showing the decreased interlayer distance upon compaction. e) Raman spectra of E-rGtO and DB-rGtO, demonstrating the attenuation of G band signal upon compaction.

The packing density of the material increases more than threefold, from 0.53 g·cm^{-3} for E-rGtO to 1.69 g·cm^{-3} for DB-rGtO. This packing density falls within the typical range reported for densified carbon-based materials (0.7–1.9 g·cm^{-3}) (Table S2). Notably, compacted graphene-like sheets remain visibly exposed on the surfaces of the DB-rGtO particles. The lateral size and thickness distribution of DB-rGtO is shown in Figure 1c. The lateral dimensions are predominantly within 1–10 μm, with an average size of 5.96 μm, while thicknesses range from 0.1–1 μm, averaging 0.85 μm. Based on these dimensions, DB-rGtO particles can be approximated as oblate spheroids with an aspect ratio of approximately 0.1. This three-dimensional dense structure, combined with the surface-exposed graphene-like sheets, imparts unique solvent-interactive and rheological properties that distinguish DB-rGtO from well-studied materials such as fully exfoliated 2D graphene, graphene nanoplatelets, or conventional graphite. These distinctive characteristics are examined in detail in the subsequent sections of this work.

X-ray diffraction (XRD) and Raman spectroscopy analyses of E-rGtO and DB-rGtO are presented in Figures 1d and 1e, respectively. In the XRD patterns, both samples exhibit crystalline characteristics with pronounced (002) diffraction peaks, typical of graphitic materials. For E-rGtO, the (002) peak appears at 21.69°, indicating a relatively expanded stacked structure with an interlayer distance of d = 0.409 nm. In contrast, DB-rGtO shows a peak shift to 25.35°, corresponding to a reduced interlayer spacing of d = 0.351 nm. This shift, along with the increased peak intensity, confirms the formation of a denser, more compact structure. However, the interlayer distance in DB-rGtO remains larger than that of pristine graphite or graphene nanoplatelets (~ 0.335 nm) [33, 34]. Raman spectra of both E-rGtO and DB-rGtO reveal prominent features associated with structural disorder, deconvoluted into first-order modes of D, D’, D”, D* and G bands [35]. Both spectra are characterised by a

distinct G band at ~ 1590 cm^{-1}, associated with the E_{2g} vibration mode of the graphitic lattice, and a D band at ~ 1350 cm^{-1}, attributed to the A_{1g} breathing mode of sp^2 carbon atoms within aromatic rings [36, 37]. The intensity ratio of the D to G band (I_D/I_G) is commonly employed to quantify defect density in carbon-based materials. The initial thermal expansion introduced significant lattice defect, as evidenced by an I_D/I_G ratio of 2.55. Following the ball-milling step, this ratio further increases to 3.24, primarily due to the reduced intensity of the G peak. We further compared the full width at half maximum (FWHM) of the D bands of both materials, noticing negligible difference, with values of 153.5 cm^{-1} for E-rGtO and 137.5 cm^{-1} for DB-rGtO. This similarity in D band broadening suggests both materials possess a comparably high defect density and structural disorder characteristic of thermally reduced graphite oxide. The attenuation of the G band signal after ball-milling can be attributed to mechanical collisions that fragment the graphitic sheets into smaller domains, thereby disrupting the crystalline sp^2 network and diminishing lattice coherence [38]. Furthermore, the presence of a D" band at ~ 1540 cm^{-1} confirms the existence of an amorphous carbon phase in both samples [35]. In addition, FTIR and XPS analysis confirm the reduced graphite oxide nature of both E-rGtO and DB-rGtO (Figure S5 and S6).

2.2 Analysis of solvated microstructures using quantitative polarised light microscopy

Understanding the solvent-interactive behaviour of DB-rGtO is essential for elucidating the rheological properties of its dispersions, which in turn supports the rational design and formulation of printable inks. To investigate this, four environmentally benign solvents were selected for the study of the dispersions: water, terpineol, dihydrolevoglucosenone (commonly known as Cyrene), and dibasic ester (DBE). All of these solvents have been previously reported in the literature for their compatibility with graphene processing and

printing applications [27, 39-46]. To investigate the microstructures of DB-rGtO in various solvents, we employed two complementary imaging techniques: (1) quantitative polarised light imaging (retardance imaging) to visualise thin-sheet microstructures, and (2) brightfield imaging to capture denser and/or thicker structures. Retardance imaging is based on automated polarisation control and quantification, utilising electronically controlled variable retarder plates, a polariser/analyser setup, and a computer algorithm. This system enables simultaneous detection and quantification of all types of microstructures present in the dispersion (Figure S7).

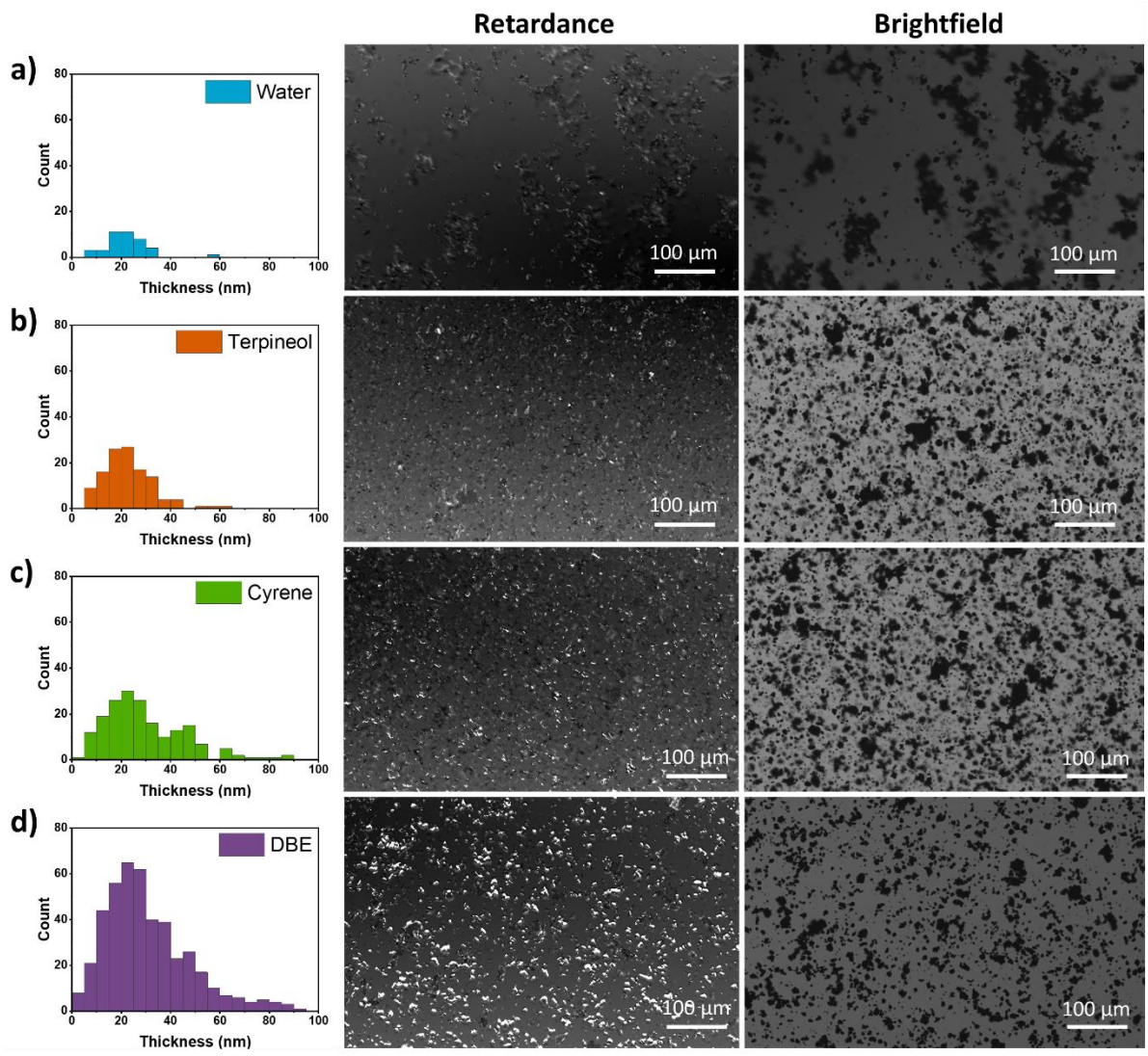

Figure 2: Distribution of the thicknesses (nm) of solvated microstructures, deduced from the optical retardance from retardance images; while brightfield images measure the level of unsolvated or agglomerated microstructures in the DB-rGtO dispersions (10 mg·mL^{-1}) in all solvents: a) water, b) terpineol, c) Cyrene and d) DBE.

A key advantage of this imaging method is that it does not require specialised sample preparation, unlike techniques such as SEM or AFM [47]. This enables accurate, *in situ* estimation of both thin-sheet species (e.g., fully exfoliated structures) and thicker species (e.g., unexfoliated or agglomerated structures) within the same dispersion. Our group has previously developed this methodology for identifying and quantifying graphene- and graphene oxide–based dispersions, whether synthesised in the laboratory or sourced commercially [48, 49]. Owing to their birefringent nature, graphene-like sheets transmit polarised light and appear as regions of high contrast in grayscale retardance images. The observed brightness corresponds to the optical retardance of the particles, which can be quantitatively linked to their thickness (Section S2, SI).

Polarised light microscopy was performed on DB-rGtO dispersions at a relatively low concentration (10 mg·mL^{-1}) to enable clear visualisation of the samples (Figure 2). In their non-solvated state, the thick, three-dimensional DB-rGtO particles are optically isotropic and remain dark in retardance imaging. However, upon solvation, solvent penetration swells the graphene-derived blocks and realigns the surface layers, resulting in solvated, thin-sheet microstructures. These solvated microstructures are optically-anisotropic (birefringent), appear bright in retardance imaging [49]. Retardance images and brightfield images respectively provide complementary views of solvated and unsolvated particles. The extent of DB-rGtO solvation in each solvent was quantified by evaluating both the count of

birefringent (solvated) particles and the broadness of their thickness distribution derived from retardance imaging.

In water-based dispersions, only a small number of solvated particles were observed, accompanied by a narrow thickness distribution, indicating negligible solvation of DB-rGtO. Retardance images showed minimal birefringence, primarily originating from the thin edges of large, unsolvated aggregates, while brightfield images confirmed the dominance of thick, highly light-absorbing microstructures (Figure 2a). In contrast, DB-rGtO dispersions in terpineol, Cyrene, and DBE displayed significantly enhanced solvation behaviour. Specifically, DB-rGtO in terpineol and Cyrene exhibited nearly identical thickness distributions with moderate levels of birefringence, suggesting intermediate degrees of solvation (Figures 2b and 2c). Among the tested solvents, DBE induced the strongest solvation effect, as evidenced by substantially higher optical retardance and a broader, upper-skewed thickness distribution (Figure 2d), indicating a large number of well-solvated particles. Furthermore, while DB-rGtO particles exhibited a high degree of agglomeration in water, brightfield images of terpineol-, Cyrene-, and DBE-based dispersions revealed markedly improved dispersibility, with agglomerated structures present in significantly smaller lateral sizes. Overall, quantification of the microstructures, including their dimensions and frequency, provides crucial insights into the solvent-dependent solvation behaviour of DB-rGtO.

As a control experiment, we investigated the microstructures of graphene nanoplatelets (GNP) dispersions prepared under the same conditions. GNPs exhibit a block-like morphology comparable to that of DB-rGtO; however, unlike DB-rGtO, the graphene layers in GNPs are tightly bound and do not undergo solvation in the tested solvents. This contrast highlights the

distinct microstructural and interaction properties of DB-rGtO compared to conventional layered graphene materials (Figure S8).

DB-rGtO solvation within dispersions is primarily governed by two intrinsic solvent properties: surface tension and viscosity, both of which impact wettability and capillary action. Effective wettability is essential for initiating particle solvation, as it enables solvent molecules to penetrate the compacted graphene-block layers. Solvents with relatively low surface tension, such as terpineol, Cyrene, and DBE, exhibit adequate wettability on the DB-rGtO surface, thereby promoting solvation. In contrast, water, owing to the high surface tension, demonstrates poor wettability, which restricts solvent infiltration and results in negligible DB-rGtO solvation. Once solvation begins, capillary action determines how efficiently the solvent propagates within the DB-rGtO structure. Here, solvent viscosity plays a critical role: low-viscosity solvents, such as DBE, facilitate easier solvent movement and thus stronger solvation compared to more viscous solvents like terpineol and Cyrene.

As a thermally reduced graphite oxide material, DB-rGtO contains several oxygen functional groups, as confirmed by FTIR analysis (Figure S5), which overall improves its wettability in polar media and markedly enhances dispersibility compared to pristine graphite/graphene. These functional groups introduce polarity to the graphene surface, thereby strengthening its affinity towards polar solvents. Such interfacial interactions effectively promote wettability and suppress agglomeration, yielding stable dispersions [50, 51]. Notably, all solvents examined in this study are polar in nature, thus facilitating the dispersibility of DB-rGtO. In addition, we examine the role of hydrogen bonding based on solvent molecule structures. Specifically, the presence of functional groups exerts pronounced effect on water and terpineol, as both solvents possess OH group that can act as hydrogen bond donor and

acceptor, readily forming extensive hydrogen-bonding interactions with DB-rGtO [52, 53]. In contrast, the contribution of hydrogen bonding is less significant in Cyrene and DBE. The ketone group in Cyrene, and the ester groups in DBE suggests that those solvents predominantly act as hydrogen bond acceptors, not donors [54]. Despite this, our results showed that DB-rGtO agglomerate markedly in water, whereas improved dispersibility is observed in terpineol, Cyrene, and DBE. These findings indicate that the overall dispersibility of DB-rGtO is not solely determined by functional groups, but rather by multiple factors including solvent surface tension, solvent viscosity, and Hansen solubility parameters (HSPs).

Previous studies have shown that the Hansen Solubility Parameters (HSPs) of a solvent are crucial in determining whether graphene-based materials remain dispersed or tend to aggregate [1, 55]. The severe agglomeration observed in water-based DB-rGtO dispersions can be attributed to the significant mismatch between water's HSPs and the optimal values for dispersing graphene. Conversely, terpineol, Cyrene, and DBE, commonly used solvents in graphene printing, exhibit better alignment with these HSPs, resulting in reduced agglomeration. To further validate these findings, DB-rGtO dispersions were prepared using three additional solvents: propylene carbonate (PC), ethanol, and isopropanol (IPA), and analysed via polarised light microscopy (Figure S9). These solvents, characterised by low surface tension and low viscosity, facilitated strong DB-rGtO solvation, as indicated by abundant birefringence in retardance images. However, pronounced agglomeration was also observed, consistent with their substantial HSP mismatches with graphene. Overall, DB-rGtO solvation is predominantly dictated by solvent surface tension and viscosity, while agglomeration behaviour is largely governed by the compatibility of solvent HSPs with those

of graphene. The relevant surface tension, viscosity, and HSP values for all solvents studied and relevant to these discussions are summarised in Tables S3 and S4.

2.3 Rheological behaviours of DB-rGtO dispersions

It is well-established that the rheological properties of structured fluids critically influence the accuracy and reliability of coating and printing processes, which, in turn, impact the performance of the resulting devices. In the context of conductive inks, excessively high viscosity and elasticity can hinder smooth ink deposition, leading to uneven coverage of the active material and reduced film conductivity. Conversely, inks with insufficient viscosity and elasticity are prone to overspreading, which can compromise pattern fidelity and potentially result in electrical short circuits [23]. We employed two different concentrations, 100 and 150 $mg{\cdot}mL^{-1}$ in water, terpineol, Cyrene and DBE to prepare dispersions. We carefully selected these two concentrations as they: (i) exhibit rheological behaviour that lies between that of a Newtonian fluid and a solid—characteristic of viscoelastic structured fluids suitable for typical coating and printing processes; and (ii) demonstrate a pronounced change in rheological properties when increasing from 100 to 150 $mg{\cdot}mL^{-1}$ across the tested solvents, thereby presenting structured fluids of distinct natures.

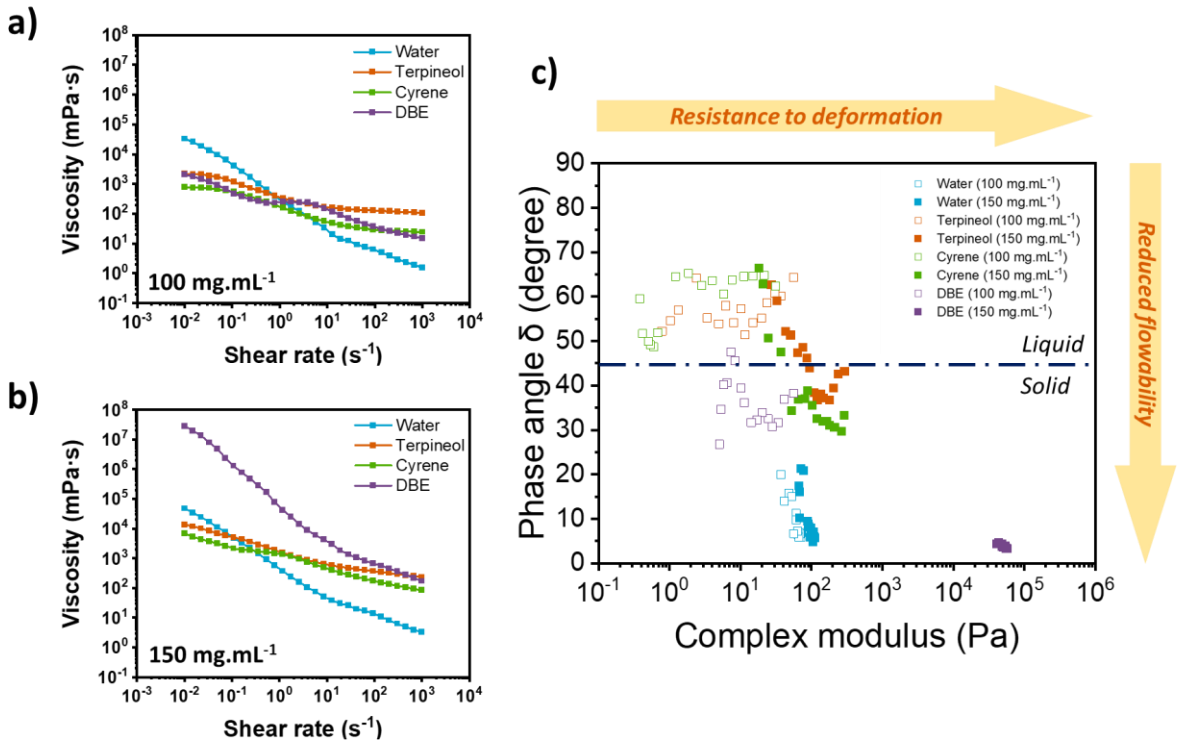

Figure 3: Rheological behaviours of DB-rGtO dispersions in different solvents (water, terpineol, Cyrene and DBE). a) Shear viscosity at 100 mg·mL^{-1}. b) Shear viscosity at 150 mg·mL^{-1}. c) Phase angle vs complex modulus graph, demonstrating the relative resistance to deformation and flowability of DB-rGtO dispersions in the four solvents.

All dispersions exhibit shear-thinning behaviour (Figure 3a and 3b), where viscosity decreases with increasing shear rate, following a power-law relationship - a rheological characteristic highly desirable for coating and printing applications [1, 23]. Polarised light microscopy reveals that DB-rGtO particles undergo negligible solvation but significant agglomeration in water. These agglomerated particles can entrap solvent molecules; however, the large void spaces surrounding them enable easy solvent escape under shear [56]. Consequently, water-based dispersions exhibit pronounced shear-thinning behaviour, characterised by high viscosity at low shear rates and a sharp viscosity drop at higher shear rates. Additionally, due to ongoing particle agglomeration with increasing concentration, water-based dispersions

display relatively high viscosity at 100 mg·mL^{-1} but only a marginal rise when the concentration increases to 150 mg·mL^{-1}. Meanwhile, the characteristics of terpineol-, Cyrene- and DBE-based dispersions are mainly governed by DB-rGtO solvation (Figure 3a, 3b and S10). In detail, DB-rGtO exhibits strong solvation in DBE. The formation of solvated layers in a large quantity considerably increases particle surface area and interparticle interactions, thereby inhibiting fluid flow and resulting in high relative viscosities. As such, DBE-based dispersions show high relative viscosity even at 100 mg·mL^{-1}, with a dramatic four-order-of-magnitude increment at 0.01 s^{-1} when the concentration increases to 150 mg·mL^{-1}. Nonetheless, the inherently low viscosity of DBE facilitates particle alignment under shear, contributing to a steep viscosity decline at higher shear rates. Terpineol- and Cyrene-based dispersions, which exhibit moderate DB-rGtO solvation, contain a mix of solvated and un-solvated particles. The high solvent viscosity restricts particle reorientation upon shearing. As a result, dispersions in both solvents show lower relative viscosities than DBE-based dispersions at low shear and only a modest reduction in viscosity at high shear. Furthermore, these systems exhibit lower relative viscosities at 100 mg·mL^{-1} and a moderate increase when the concentration is raised to 150 mg·mL^{-1}.

Oscillatory tests (Figure S11 and S12) provide insights on the elastic (*G'*) and viscous (*G"*) portions of the viscoelastic behaviours in DB-rGtO dispersions. The elastic or storage modulus (*G'*) is an indicator of the energy stored in the dispersion through stretching and extending of the microstructures, whereas the viscous or loss modulus (*G"*) specifies the frictional energy dissipating as heat during the flow. The viscous portion enables the dispersion to maintain liquid-like behaviour thus allowing it to form a coating, while the elastic portion strengthens the coated structure resulting in a compact structure after drying [23, 26]. In amplitude sweep

tests, the viscoelastic behaviours of the dispersions are characterised by a linear viscoelastic region (LVR) at a low strain rate in all solvents followed by a distinct deformation characteristic depending on the solid content and solvent media (Figure S11). During the frequency sweep measurements, the complex moduli (G^*) including the elastic (G') and viscous (G'') resistance to deformation, alongside the phase shift (δ) between the applied deformation and material response can be inferred, where $\delta = 0^o$ indicates purely elastic behaviour, and $\delta = 90^o$ corresponds to purely viscous behaviour. For better visualisation of the viscoelastic behaviours of the dispersions, we map their phase angles (δ) and complex moduli (G^*), as illustrated in Figure 3c. In general, the amplitude and frequency data strongly supplement each other. In water-based dispersions, agglomerated DB-rGtO particles considerably restricts the dispersion flowability, exhibiting solid-like characteristic, indicative from the low phase angle. Nevertheless, the easy escape of trapped solvent molecules implies easy deformation of dispersions under external shear strain/stress, represented from the relatively low complex modulus. Similar to the shear viscosity behaviour, as particles keep agglomerating, DB-rGtO dispersions at two concentrations (100 and 150 $mg \cdot mL^{-1}$) show nearly identical viscoelastic characteristics. Meanwhile, the effects of moderate to strong particle solvation are observed in terpineol-, Cyrene- and DBE-based dispersions. In all solvents, the increase of DB-rGtO concentration apparently shifts the dispersions to lower phase angle (i.e. reduced flowability) and higher complex modulus (i.e. stronger resistance to deformation), though the extent of these changes varies across solvents. In DBE, the strong particle solvation results in larger quantity of solvated particles forming more interconnected, percolated network. Compared to dispersions in terpineol and Cyrene, DBE-based dispersions exhibit slightly stronger solid-like characteristic and deformation resistance at 100 $mg \cdot mL^{-1}$, and markedly higher values at 150 $mg \cdot mL^{-1}$. At this higher concentration, the DBE-based

dispersion demonstrates a very high complex modulus at a low phase angle, indicative of gel-like behaviour. Meanwhile, moderate particle solvation in terpineol and Cyrene allows better dispersion flowability, as reflected by datapoints remaining above the liquid-solid transition at δ= 45°. In summary, rheological measurements further evidence strong DB-rGtO agglomeration yet negligible solvation in water, moderate DB-rGtO solvation in terpineol and Cyrene, and strong DB-rGtO solvation in DBE, which agrees well across steady and oscillatory tests.

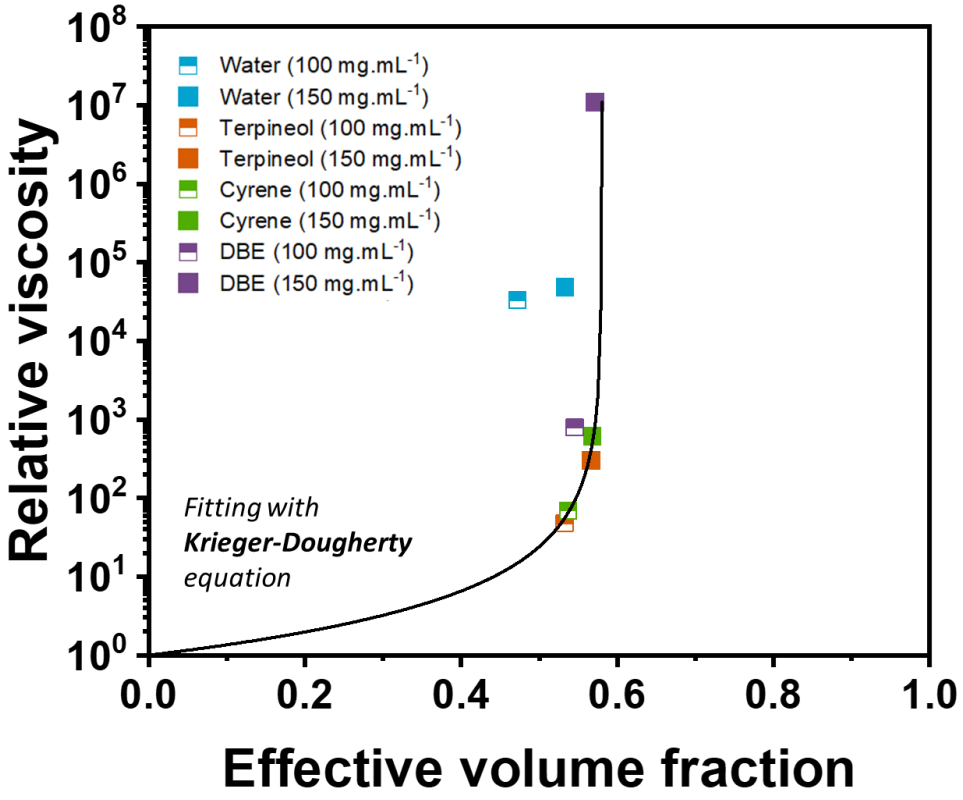

Figure 4: Estimation of DB-rGtO effective volume fractions based on polarised microscope image analysis versus the experimentally measured relative viscosities of DB-rGtO dispersions. The estimated datapoints are fitted with Krieger–Dougherty equation, showing the observed viscosities can be explained by the enhancement of effective volume via solvation.

For clarification, at the same mass concentrations of 100 and 150 mg·mL^{-1}, the rheological behaviours of DB-rGtO dispersions vary significantly depending on the solvent used. This variation can be explained by the differences in the effective volume fraction of DB-rGtO, which is influenced by how well the solvent interacts with the DB-rGtO particles (solvation behaviour). In solvents where solvation is stronger, particles tend to realign the surface layers and expand, leading to a higher effective volume fraction, and *vice versa*. In practical applications, particularly in rheology, effective volume fraction provides a more accurate representation than mass concentration, since it directly reflects the extent to which particles influence the overall behaviour of the dispersion [56, 57]. To show that variations in the effective volume fraction of DB-rGtO due to solvation can be compared across different solvents, a methodology was developed to estimate this volume fraction using images taken from polarised light microscopy (Section S4, including Figure S13-S15, SI). The estimated effective volume fractions are then plotted against the experimentally measured relative viscosities of the DB-rGtO dispersions. These data points are subsequently fitted to the well-known Krieger-Dougherty equation [58], which is commonly used to relate the viscosity of suspensions to their effective volume fraction (Figure 4). With the exception of water-based dispersions, all DB-rGtO systems show good agreement with the model. This supports the conclusion that, from moderately-solvating solvents (terpineol and Cyrene) to strongly-solvating solvents (DBE), the observed increase in viscosity can be rationalised by solvation-induced enhancement of the effective volume fraction. It is important to note that our viscosity estimation applies to the concentrated regime described by the Krieger–Dougherty model, where even small changes in effective volume fraction can significantly impact dispersion viscosity, critical for high-concentration inks used in various coating and printing methods.

The study of DB-rGtO rheological behaviours provides insights for formulating concentrated, printable DB-rGtO ink with minimal binder use. Water is unsuitable for DB-rGtO ink due to poor flowability and strong particle agglomeration. As DBE promotes strong solvation and increases the particle effective volume, it makes the dispersions prone to gelation, preventing its use for high-concentration DB-rGtO inks. In contrast, terpineol and Cyrene offer moderate solvation, making them ideal solvents for high DB-rGtO mass loading inks. These solvents provide the right balance of viscosity and flowability at high concentrations. The solvation effect in DB-rGtO dispersions distinguishes their rheological properties from other graphene materials such as graphene nanoplatelets (GNP). While DB-rGtO dispersions show significant variation in relative viscosity across solvents due to differences in particle solvation, GNP dispersions remain largely unchanged (Figure S16). Across the examined solvents, the zero-shear relative viscosities (at 0.01 s^{-1}) of DB-rGtO dispersions span over one order of magnitude at 100 mg·mL^{-1} and nearly five orders at 150 mg·mL^{-1}. In contrast, GNP dispersions vary by less than one order of magnitude at 100 mg·mL^{-1} and only about one order at 150 mg·mL^{-1}, highlighting uniform dispersion conditions for GNP uninfluenced by the solvent interactions.

2.4 Printing of concentrated, binder-free conductive DB-rGtO inks

To illustrate how DB-rGtO solvation affects ink rheology, we evolve our analysis from dispersion rheology to concentrated ink formulation, focusing on high-throughput, cost-effective screen printing. Compared to other printing techniques (inkjet, gravure, flexographic, etc.), screen printing offers the advantage of depositing relatively thick films (typically > 10 µm), making it particularly suitable for concentrated inks with high mass loading of active materials [1, 23]. As a contact-based technique, screen printing is operated by forcing the ink through a pre-patterned mesh onto the substrate using a squeegee (Figure

S17a, S17b). Given the multi-stage nature of the process, screen printing necessitates dedicated tuning of ink rheology towards uniform, high-resolution printing patterns. Generally, screen printing requires inks with higher viscosity compared to other printing techniques. A shear-thinning profile is desirable, which facilitates easy ink flow during printing while avoiding ink overspreading once printed. In details, under high-shear conditions during the printing stage (typically 100 s^{-1}), the ink viscosity should fall within the range of $2{\cdot}10^3$ mPa·s to 5.10^4 mPa·s, which guarantees sufficient ink penetration through the mesh without overspreading [23]. Under low-shear conditions associated with the post-printing levelling stage (typically 0.01 s^{-1}), the ink viscosity should be maintained between $1{\cdot}10^4$ mPa·s and 1.10^7 mPa·s [59, 60]. This ensures optimal ink levelling to merge the raised areas caused by filament formation during screen-substrate separation, while also preventing undesirable ink spreading that may degrade printing resolution [61, 62]. Figure 5a presents the theoretical viscosity ranges required for screen printing under both high-shear (100 s^{-1}) and low-shear (0.01 s^{-1}) conditions, benchmarked with three different commercial screen-printing inks.

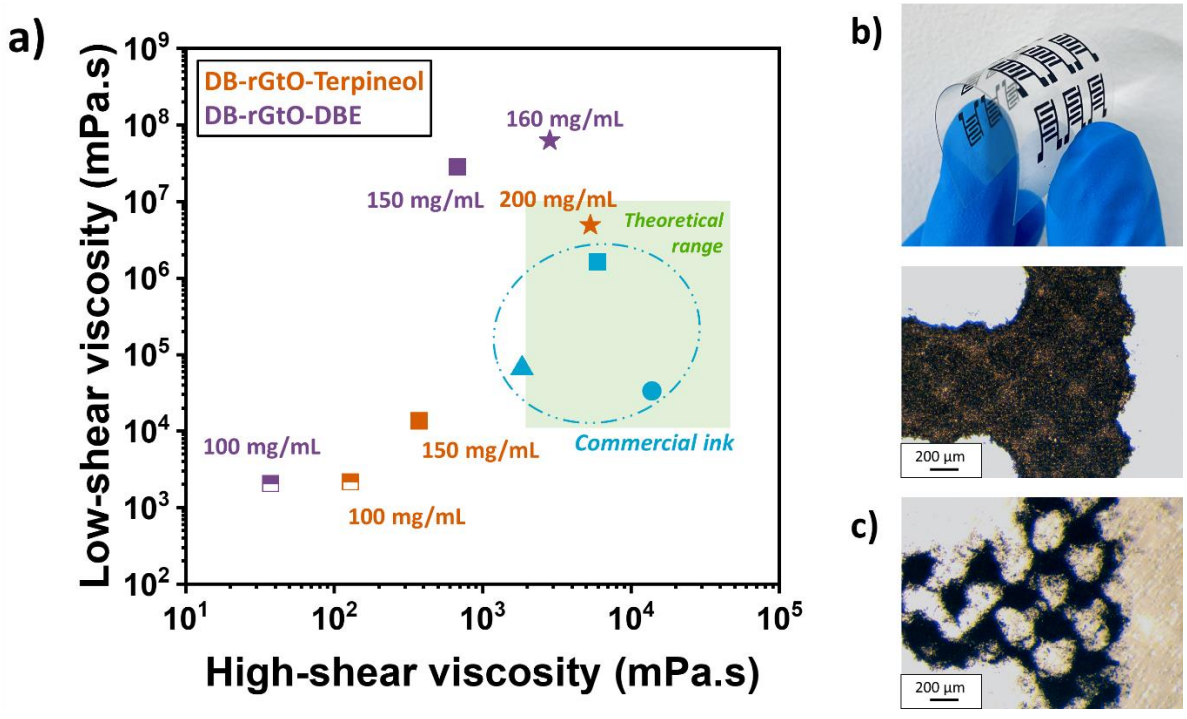

Figure 5: Leveraging solvation behaviour of DB-rGtO for screen printing of concentrated, binder-free inks. a) A graph of guidelines towards screen printing on ink rheology includes high-shear viscosity (100 s^{-1}, corresponding to ink printing stage) and low-shear viscosity (0.01 s^{-1}, corresponding to ink leveling stage). Solvation behaviour varies across systems (DB-rGtO-Terpineol and DB-rGtO-DBE) and induces diverse rheological characteristics of dispersions, enabling ink rheology tailoring without any binder used. b) Printing result of DB-rGtO-Terpineol-200, achieving miniaturised pattern with high resolution and uniform coverage. c) Printing result of DB-rGtO-DBE-160, showing mesh marking defect.

To demonstrate how varying degrees of particle solvation influence ink rheology and ultimately affect screen-printing quality, we employed two dispersion systems with distinct solvation behaviours: DB-rGtO-Terpineol (moderate solvation) and DGB-DBE (strong solvation) to conduct binder-free printing on flexible PET substrate. The DB-rGtO concentrations are adjusted to adapt the high-shear viscosity required during printing stage (above $2 \cdot 10^3$ mPa·s at 100 s^{-1}), as illustrated in Figure 5a. As such, the concentrations of DB-rGtO-Terpineol and DB-rGtO-DBE dispersions are set to 200 mg·mL^{-1} and 160 mg·mL^{-1}, respectively. These two binder-free inks are hereafter referred to as DB-rGtO-Terpineol-200 and DB-rGtO-DBE-160. It is noteworthy that at 200 mg·mL^{-1}, the DB-rGtO-DBE dispersion appears as a playdough-like material that cannot be processed (i.e. printing or rheological measuring), owing to the strong particle solvation. Data of DB-rGtO-Terpineol and DB-rGtO-DBE dispersions at 100 mg·mL^{-1} and 150 mg·mL^{-1} are also included in the graph to facilitate clearer visualisation on the relative solvation levels of DB-rGtO in each solvent. Since DB-rGtO-Terpineol-200 falls within the viscosity range for screen printing, the ink demonstrates optimal printing performance. Without any binders used, well-defined, miniaturised interdigitated patterns with high resolution – featuring line widths and gap distances in the

100s of μm – are successfully achieved with uniform film coverage (Figure 5b). Meanwhile, mesh marking defect is observed within the printing pattern of DB-rGtO-DBE-160, attributing to the high near-rest viscosity (Figure 5c). DB-rGtO-DBE system exhibits poor flowability and elevated low-shear viscosity owing to the strong particle solvation; besides, the low viscosity of DBE solvent contributes to a sharp viscosity drop under high shear. Accordingly, satisfying the high-shear viscosity requirement leads to an excessively high low-shear viscosity. This elevated near-rest viscosity restricts ink levelling after screen removal, inhibiting the merging of raised, unconnected features formed during screen-substrate separation. Consequently, mesh marking defect appears, severely affecting the printing fidelity.

We further compare the binder-free DB-rGtO-Terpineol-200 ink with several reported graphene inks for screen printing (Table S10). Unlike conventional graphene inks that require binders to boost concentration and tailor rheology for printability, DB-rGtO-Terpineol-200 achieves excellent screen-printing performance at a high concentration of 200 $mg \cdot mL^{-1}$ without any binder. This is enabled by the unique solvation behaviour of the compacted graphene-derived blocks, where the solvent-dependent solvation results in pronounced variations in dispersion rheology, allowing broad tunability of ink properties. Notably, DB-rGtO dispersions offer a rare combination of high concentration with low viscosity, thanks to their dense-block structure. This allows for maximum active material loading, which is crucial for high-performance devices, while retaining sufficient flowability for a wide range of coating and printing techniques. To highlight this property, we compare the concentrations of DB-rGtO dispersions with previously reported ultrahigh-concentrated graphene dispersions (Figure S18). Remarkably, at comparable dispersion viscosities, DB-rGtO concentrations exceed the highest values reported for 2D graphene inks in the literature, even for DBE-based dispersions, where strong solvation significantly increases viscosity. We further demonstrate

the versatility of DB-rGtO ink, in particular, the DB-rGtO-Terpineol system, by extending its application to various deposition techniques, including blade coating and flexographic printing (Figure S19). This underscores the potential of formulating high-concentration graphene-based inks with little to no additives for advanced printing technologies.

Compacting graphene-based materials into a dense-block structure inevitably compromises electrical conductivity, owing to the breakage of conductive graphene network resulting from ball-milling [63]. It is important to notice that the sheet resistance of the DB-rGtO film is dependent on the bulk conductivity of the starting E-rGtO. To emphasise the generality of this particle-engineering approach, we prepared binder-free inks from a more conductive precursor, N-doped E-rGtO, which is fivefold more than E-rGtO (Figure S20a) [64]. The ball-milled product retains the dense-block structure with compacted graphene-like sheets on particle surface (Figure S20b), and demonstrates solvation effects (Figure S21) unremarkable from our previous observations. Following a similar processing route (binder-free ink formulation and screen printing), the N-doped DB-rGtO conductive film exhibit a sheet resistance of approximately 7 $\Omega.\square^{-1}$ after a single pass of printing, which is around two orders of magnitude lower than that of the undoped counterpart (Table S11). Compared to other reported works, the N-doped DB-rGtO pattern (1x3 cm) exhibits excellent electrothermal performance when applied as a flexible heater, achieving temperature beyond 200^{o}C within 20 s under 10V (Figure S20c, S20d).

3. Conclusion

We have developed a new engineered form of graphene-derived material, Dense-block reduced Graphite oxide (DB-rGtO), as an active material for preparing dispersions in various printing solvents. Polarised light microscopy analysis and rheological study reveal the solvent-

dependent solvation behaviour of DB-rGtO, which distinctly set it apart from conventional, well-studied graphene-based materials. This solvent-interactive behaviour enables diverse rheological characteristics of dispersions, showing the potential of tailoring ink properties for specific coating and printing techniques with minimal additive involvement. Following these insights, a high-concentration, binder-free DB-rGtO ink is formulated, achieving high-resolution printing of miniaturised patterns on flexible substrates. The conductive DB-rGtO films are characterised in terms of electrothermal response, revealing the potential of DB-rGtO material in flexible device application. The study establishes general design principles towards formulating concentrated, binder-free graphene inks for advanced printed electronics.

4. Experimental section

DB-rGtO powder synthesis: Commercial graphite oxide (GtO) was purchased from The Sixth Element (Changzhou) Materials Technology Co. Ltd., which was then reduced *via* thermal expansion and annealing at 900^{o}C to produce expanded reduced graphite oxide (E-rGtO). The dense-block reduced graphite oxide (DB-rGtO) is prepared from the ball-milling process. 10 g of the as-prepared E-rGtO and 600 g of Zirconia balls were milled in a 500 mL jar using the planetary ball-milling machine (Pulverisette 6, Fritsch) at a rotation speed of 300 rpm for 1 hour.

Material Characterisations: The packing densities of E-rGtO and DB-rGtO were deduced following a procedure that have previously been reported [65]. In details, the powdered sample was compressed into a platelet inside a cylindrical mould (inner diameter of 1 cm). The packing density of the material was then calculated based on the weight and thickness of the platelet. The powder conductivities of the samples are measured using the powder-

pressing method [66, 67], the electrical current and voltage are controlled by a source meter (Keithley 6430 SUB-FEMTOAMP). The E-rGtO and DB-rGtO samples were then characterised by SEM (FEI Nova nano SEM 450 FEG and Thermo Scientific Verios 5 UC FEGSEM), XRD (Bruker D8 Advance Eco Diffractometer XRD), Raman (Renishaw Confocal micro-Raman Spectrometer) and FTIR (Perkin Elmer Spectrum Two, UATR accessory). The lateral size and thickness of DB-rGtO particles are quantified based on the manual measurements from SEM images using ImageJ software.

Dispersion preparation: The dispersions were prepared by mixing the powdered sample and solvent in a vacuum mixer (MSK-SFM-16, MTI Corporation) at 600 rpm for 1 hour. The solvents were all purchased from Sigma Aldrich – dibasic ester i.e. DBE (Product No: 422053), terpineol (Product No: 86420), dihydrolevoglucosenone i.e. Cyrene (Product No: 807796). Regarding GNP dispersions, GNP powder was purchased from Sigma Aldrich (Product No: 900407). Dispersion concentrations can be monitored by adjusting the amount of solvent.

Polarised light microscopy analysis: Liquid-Crystalline PolScope i.e. LC-Polscope (optical train is described in Figure S7b) facilitated fast and label-free quantification of the optical retardance and slow-axis orientation of DB-rGtO particles at the highest resolution. This method does not require mechanical rotation or movement of the specimen or microscope parts during image acquisition. Instead, a universal compensator comprising a linear polariser and two-variable retarder plates called LC-A and LC-B replaces the traditional compensator. The retarders are uniformly birefringent LC plates whose optical properties are controlled by electro-optical devices. Before each experiment, a calibration procedure was performed to remove the background retardance by capturing a background image from a sample-free area. For a particular area of interest in the specimen, the microscope generated one

circularly-polarised, and four elliptically-polarised images from the predetermined retarder settings of LC-A and LC-B. A CCD camera captured the raw images and an algorithm instantaneously computed the retardance and slow-axis orientation maps. Monochromatic illumination (546 nm) was used and the exposure time was kept constant throughout all imaging. For a brightfield measurement, the polariser and the analyser were removed from the optical path. After adjusting the light intensity, a brightfield image was captured for the same area of interest [68, 69].

Rheological measurements: Rheology characterisations were carried out using a rheometer (MCR302, Anton Paar) with a cone-plate geometry. Typically, 0.6 mL of dispersion/ink was dropped to the bottom plate. Throughout the measurements, the rheometer kept a constant temperature of 25.00 ± 0.01 °C and a constant cone-plate gap of 1 mm. Shear viscosity measurements were performed within a shear rate range of 0.01 – 1000 s^{-1}. Amplitude sweep tests were performed in a shear strain range of 0.001 – 100% under an angular frequency of 10 Hz (20π rad·s^{-1}). Frequency sweep tests were performed at 0.01% shear strain for all the dispersions (i.e. within the linear viscoelastic regions determined from the amplitude sweep tests) in an angular frequency range of 0.01 – 100 rad·s^{-1}.

Printing of concentrated, binder-free inks: Screen printing was performed using a multifunctional printer (C650, NSM Norbert Schlafi AG) at a printing speed of 4 m.min^{-1} and a snap-off distance of 0.5 mm. A 47S screen (equivalent to the mesh opening size of 150 µm) is used for the process. Polyethylene terephthalate (PET) (thickness of 125 µm) and polyimide (PI) (thickness of 150 µm) are employed as printing substrates. After printing, the wet printed samples are dried at 120^{o}C in a vacuum oven overnight. Given the binder-free nature of the printed samples, the film adhesion on substrate is achieved by compression rolling, with a

rolling gap of 100 µm. Apart from the formulated DB-rGtO inks, three different commercial inks are used in the experiment to better benchmark the viscosity requirements of high-quality screen printing: DM-SIP-3060S, Dycotec Materials (denoted as Commercial ink 1, SI); DM-CAP-4511S, Dycotec Materials (denoted as Commercial ink 2, SI); Series 552-9083, Printcolor (denoted as Commercial ink 3, SI). The printing features are characterised under optical microscope (DFK 33GP1300e, The Imaging Source). The sheet resistance was measured by the 4-point probe method using a source meter (Keithley 6430 SUB-FEMTOAMP) and a 4-point probe head (SR-4, Everbeing Intl Corp). The film thickness was measured by a micrometre screw gauge. For the electrothermal measurement of the screen-printed conductive film (1 x 3 cm), a voltage power source was connected to the film *via* two probes, allowing the Joule heating. The temperature change of the film was captured by an infrared camera (FLIR i7, Teledyne FLIR).

5. Acknowledgement

This work was supported by the Australian Research Council (ARC) and Ionic Industries Pty Ltd through the ARC Research Hub for Advanced Manufacturing with 2D Materials (IH210100025). The authors gratefully acknowledge the use of equipment and the scientific and technical support provided by Timothy Williams at the Monash Centre for Electron Microscopy (MCEM), part of the Victorian Node of Microscopy Australia. We also acknowledge Ms Yvonne Hora for her assistance and the use of facilities at the Monash X-ray Platform.

6. Conflict of Interest

The authors declare no conflict of interest.

7. Reference

1. Hu, G.H., et al., *Functional inks and printing of two-dimensional materials.* Chemical Society Reviews, 2018. **47**(9): p. 3265-3300.
2. Tran, T.S., N.K. Dutta, and N.R. Choudhury, *Graphene inks for printed flexible electronics: Graphene dispersions, ink formulations, printing techniques and applications.* Advances in Colloid and Interface Science, 2018. **261**: p. 41-61.
3. Jafarpour, M., et al., *Functional Ink Formulation for Printing and Coating of Graphene and Other 2D Materials: Challenges and Solutions.* Small Science, 2022. **2**(11).
4. Hernandez, Y., et al., *High-yield production of graphene by liquid-phase exfoliation of graphite.* Nature Nanotechnology, 2008. **3**(9): p. 563-568.
5. Li, D., et al., *Processable aqueous dispersions of graphene nanosheets.* Nature Nanotechnology, 2008. **3**(2): p. 101-105.
6. Derjaguin, B. and L. Landau, *Theory of the Stability of Strongly Charged Lyophobic Sols and of the Adhesion of Strongly Charged-Particles in Solutions of Electrolytes.* Progress in Surface Science, 1993. **43**(1-4): p. 30-59.
7. Verwey, E.J.W., *Theory of the Stability of Lyophobic Colloids.* Journal of Physical and Colloid Chemistry, 1947. **51**(3): p. 631-636.
8. Dong, L., et al., *A non-dispersion strategy for large-scale production of ultra-high concentration graphene slurries in water.* Nature Communications, 2018. **9**.
9. Xiong, Z.Y., et al., *Ultrahigh concentration exfoliation and aqueous dispersion of few-layer graphene by excluded volume effect.* Nature Communications, 2024. **15**(1).
10. He, P., et al., *Processable Aqueous Dispersions of Graphene Stabilized by Graphene Quantum Dots.* Chemistry of Materials, 2015. **27**(1): p. 218-226.
11. Park, H.J., et al., *Fluid-Dynamics-Processed Highly Stretchable, Conductive, and Printable Graphene Inks for Real-Time Monitoring Sweat during Stretching Exercise.* Advanced Functional Materials, 2021. **31**(21).
12. Cui, J.S. and S.X. Zhou, *High-Concentration Self-Cross-Linkable Graphene Dispersion.* Chemistry of Materials, 2018. **30**(15): p. 4935-4942.
13. Wajid, A.S., et al., *Polymer-stabilized graphene dispersions at high concentrations in organic solvents for composite production.* Carbon, 2012. **50**(2): p. 526-534.
14. Khan, U., et al., *Solvent-Exfoliated Graphene at Extremely High Concentration.* Langmuir, 2011. **27**(15): p. 9077-9082.
15. Khan, U., et al., *High-Concentration Solvent Exfoliation of Graphene.* Small, 2010. **6**(7): p. 864-871.
16. Liu, W., et al., *Fast Production of High-Quality Graphene via Sequential Liquid Exfoliation.* Acs Applied Materials & Interfaces, 2015. **7**(49): p. 27027-27030.
17. Paton, K.R., et al., *Scalable production of large quantities of defect-free few-layer graphene by shear exfoliation in liquids.* Nature Materials, 2014. **13**(6): p. 624-630.
18. Tran, T.S., et al., *High shear-induced exfoliation of graphite into high quality graphene by Taylor-Couette flow.* Rsc Advances, 2016. **6**(15): p. 12003-12008.
19. Liu, L., et al., *A green, rapid and size-controlled production of high-quality graphene sheets by hydrodynamic forces.* Rsc Advances, 2014. **4**(69): p. 36464-36470.
20. Nacken, T.J., et al., *Delamination of graphite in a high pressure homogenizer.* Rsc Advances, 2015. **5**(71): p. 57328-57338.
21. Varrla, E., et al., *Turbulence-assisted shear exfoliation of graphene using household detergent and a kitchen blender.* Nanoscale, 2014. **6**(20): p. 11810-11819.
22. Claypole, A., et al., *Rheology of high-aspect-ratio nanocarbons dispersed in a low-viscosity fluid.* Journal of Coatings Technology and Research, 2020. **17**(4): p. 1003-1012.
23. Abdolhosseinzadeh, S., et al., *Perspectives on solution processing of two-dimensional MXenes.* Materials Today, 2021. **48**: p. 214-240.

24. White, K.L., et al., *Effects of aspect ratio and concentration on rheology of epoxy suspensions containing model plate-like nanoparticles.* Physics of Fluids, 2015. **27**(12).
25. Zhang, B.Q., et al., *Stable dispersions of reduced graphene oxide in ionic liquids.* Journal of Materials Chemistry, 2010. **20**(26): p. 5401-5403.
26. Abdolhosseinzadeh, S., et al., *A Universal Approach for Room-Temperature Printing and Coating of 2D Materials.* Advanced Materials, 2022. **34**(4).
27. Liu, L.X., et al., *Highly conductive graphene/carbon black screen printing inks for flexible electronics.* Journal of Colloid and Interface Science, 2021. **582**: p. 12-21.
28. Luo, J.Y., et al., *Compression and Aggregation-Resistant Particles of Crumpled Soft Sheets.* Acs Nano, 2011. **5**(11): p. 8943-8949.
29. Kim, J., et al., *Tuning the hierarchical pore structure of graphene oxide through dual thermal activation for high-performance supercapacitor.* Scientific Reports, 2021. **11**(1).
30. Chen, P.Y., et al., *From Flatland to Spaceland: Higher Dimensional Patterning with Two-Dimensional Materials.* Advanced Materials, 2017. **29**(23).
31. Huang, J.X., *Self-dispersed crumpled graphene balls in oil for friction and wear reduction.* Abstracts of Papers of the American Chemical Society, 2016. **252**.
32. Mao, B.S., et al., *Hierarchical Nanohybrids with Porous CNT-Networks Decorated Crumpled Graphene Balls for Supercapacitors.* Acs Applied Materials & Interfaces, 2014. **6**(12): p. 9881-9889.
33. Ji, K.M., et al., *Lithium intercalation into bilayer graphene.* Nature Communications, 2019. **10**.
34. Geng, Y., S.J. Wang, and J.K. Kim, *Preparation of graphite nanoplatelets and graphene sheets.* Journal of Colloid and Interface Science, 2009. **336**(2): p. 592-598.
35. López-Díaz, D., et al., *Evolution of the Raman Spectrum with the Chemical Composition of Graphene Oxide.* Journal of Physical Chemistry C, 2017. **121**(37): p. 20489-20497.
36. Ferrari, A.C., *Raman spectroscopy of graphene and graphite: Disorder, electron-phonon coupling, doping and nonadiabatic effects.* Solid State Communications, 2007. **143**(1-2): p. 47-57.
37. Ferrari, A.C., et al., *Raman spectrum of graphene and graphene layers.* Physical Review Letters, 2006. **97**(18).
38. Wu, J.B., et al., *Raman spectroscopy of graphene-based materials and its applications in related devices.* Chemical Society Reviews, 2018. **47**(5): p. 1822-1873.
39. Hyun, W.J., et al., *High-Resolution Patterning of Graphene by Screen Printing with a Silicon Stencil for Highly Flexible Printed Electronics.* Advanced Materials, 2015. **27**(1): p. 109-115.
40. Hyun, W.J., et al., *All-Printed, Foldable Organic Thin-Film Transistors on Glassine Paper.* Advanced Materials, 2015. **27**(44): p. 7058-+.
41. Secor, E.B., et al., *Gravure Printing of Graphene for Large-Area Flexible Electronics.* Advanced Materials, 2014. **26**(26): p. 4533-+.
42. Shi, X.Y., et al., *Ultrahigh-voltage integrated micro-supercapacitors with designable shapes and superior flexibility.* Energy & Environmental Science, 2019. **12**(5): p. 1534-1541.
43. Pan, K.W., et al., *Sustainable production of highly conductive multilayer graphene ink for wireless connectivity and IoT applications.* Nature Communications, 2018. **9**.
44. Zhou, X.Y., et al., *A sustainable approach towards printed graphene ink for wireless RFID sensing applications.* Carbon, 2024. **218**.
45. Tagliaferri, S., et al., *Aqueous Inks of Pristine Graphene for 3D Printed Microsupercapacitors with High Capacitance.* Acs Nano, 2021. **15**(9): p. 15342-15353.
46. Karagiannidis, P.G., et al., *Microfluidization of Graphite and Formulation of Graphene-Based Conductive Inks.* Acs Nano, 2017. **11**(3): p. 2742-2755.
47. Kumar, P., et al., *Rheological properties of graphene oxide liquid crystal.* Carbon, 2014. **80**: p. 453-461.
48. Abedin, M.J., et al., *Graphene Oxide Liquid Crystal Domains: Quantification and Role in Tailoring Viscoelastic Behavior.* Acs Nano, 2019. **13**(8): p. 8957-8969.

49. Abedin, M.J., et al., *A High Throughput and Unbiased Machine Learning Approach for Classification of Graphene Dispersions.* Advanced Science, 2020. **7**(20).
50. Xia, Z.Y., et al., *Dispersion Stability and Surface Morphology Study of Electrochemically Exfoliated Bilayer Graphene Oxide.* Journal of Physical Chemistry C, 2019. **123**(24): p. 15122-15130.
51. Liu, W. and G. Speranza, *Tuning the Oxygen Content of Reduced Graphene Oxide and Effects on Its Properties.* Acs Omega, 2021. **6**(9): p. 6195-6205.
52. Wan, Q.P. and B.C. Thompson, *Control of Properties through Hydrogen Bonding Interactions in Conjugated Polymers.* Advanced Science, 2024. **11**(8).
53. Trevisan, L., A.D. Bond, and C.A. Hunter, *Relationship between interaction geometry and cooperativity measured in H-bonded networks of hydroxyl groups.* Chemical Science, 2025. **16**(17): p. 7418-7423.
54. Bohm, H.J., et al., *Oxygen and nitrogen in competitive situations: Which is the hydrogen-bond acceptor?* Chemistry-a European Journal, 1996. **2**(12): p. 1509-1513.
55. Hernandez, Y., et al., *Measurement of Multicomponent Solubility Parameters for Graphene Facilitates Solvent Discovery.* Langmuir, 2010. **26**(5): p. 3208-3213.
56. Willenbacher, N. and K. Georgieva, *Rheology of Disperse Systems.* Product Design and Engineering: Formulation of Gels and Pastes, 2013: p. 7-49.
57. Mueller, S., E.W. Llewellin, and H.M. Mader, *The rheology of suspensions of solid particles.* Proceedings of the Royal Society a-Mathematical Physical and Engineering Sciences, 2010. **466**(2116): p. 1201-1228.
58. Krieger, I.M. and T.J. Dougherty, *A Mechanism for Non-Newtonian Flow in Suspensions of Rigid Spheres.* Transactions of the Society of Rheology, 1959. **3**: p. 137-152.
59. Potts, S.J., et al., *The influence of carbon morphologies and concentrations on the rheology and electrical performance of screen-printed carbon pastes.* Journal of Materials Science, 2022. **57**(4): p. 2650-2666.
60. Sergent, J.E., *Screen Printing*, in *Ceramic Interconnect Technology Handbook*. 2007, Taylor & Francis Group.
61. Potts, S.J., et al., *The Effect of Carbon Ink Rheology on Ink Separation Mechanisms in Screen-Printing.* Coatings, 2020. **10**(10).
62. Zavanelli, N. and W.H. Yeo, *Advances in Screen Printing of Conductive Nanomaterials for Stretchable Electronics.* Acs Omega, 2021. **6**(14): p. 9344-9351.
63. Dong, Y., et al., *Boosting the Electrical Double-Layer Capacitance of Graphene by Self-Doped Defects through Ball-Milling.* Advanced Functional Materials, 2019. **29**(24).
64. Olalekan Solomon Oluwole, P.J., Shadhon Chandra Mohonta, Tuan Kien Nguyen, Phillip Aitchison, Nemai C. Karmakar, Mainak Majumder, *Low-temperature graphitization by amine-assisted combustion of graphene oxide.* npj 2D Materials and Applications, 2025.
65. Dong, Y., et al., *Modulating the defects of graphene blocks by ball-milling for ultrahigh gravimetric and volumetric performance and fast sodium storage.* Energy Storage Materials, 2020. **30**: p. 287-295.
66. Celzard, A., et al., *Electrical conductivity of carbonaceous powders.* Carbon, 2002. **40**(15): p. 2801-2815.
67. Marinho, B., et al., *Electrical conductivity of compacts of graphene, multi-wall carbon nanotubes, carbon black, and graphite powder.* Powder Technology, 2012. **221**: p. 351-358.
68. Oldenbourg, R. and G. Mei, *New Polarized-Light Microscope with Precision Universal Compensator.* Journal of Microscopy-Oxford, 1995. **180**: p. 140-147.
69. Oldenbourg, R., *A new view on polarization microscopy.* Nature, 1996. **381**(6585): p. 811-812.